REFERENCES

1. M. Vera-Isasa, Antenas de ranuras en guía radial: Análisis, diseño y aplicaciones, doctoral dissertation, Universidade de Vigo, Spain, 1996.
2. M. Ando, New DBS receiver antennas, Proc Euro Microwave Conf (1994), 84–92.
3. J. Takada, M. Ando, and N. Goto, A reflection canceling slot set in a linearly polarized radial line slot antenna, IEEE Trans Antennas Propagat AP-40 (1992), 433–438.
4. M. Ando, K. Sakurai, N. Goto, K. Arimura, and Y. Ito, A radial line slot antenna for 12 GHz satellite TV reception, IEEE Trans Antennas Propagat AP-33 (1985), 1347–1353.
5. A. Akiyama, T. Yamamoto, M. Ando, and E. Takeda, Conical beam radial line slot antennas for 60 GHz band wireless LAN, IEEE AP-S 3 (1998), 1421–1424.
6. M. Sierra-Pérez, J.M. Salamanca, M. Vera-Isasa, and M. Sierra-Castañer, Synthesis of circularly polarised multiprobe feed radial line slot antenna, IEEE AP-S 2 (1998), 1184–1187.
7. M. Sierra-Castañer, M. Sierra-Pérez, and M. Vera-Isasa, Design of monopulse radial line slot antennas, IEEE AP-S 4 (1999), 2774–2777.
8. M. Sierra-Pérez, M. Vera-Isasa, A.G. Pino, and M. Sierra-Castañer, Analysis of slot antennas on a radial transmission line, Int J MiMi CAE 6 (1996), 115–127.
9. M. Sierra-Perez, J.M. Salamanca, M. Vera-Isasa, and M. Sierra-Castañer, Synthesis of circularly polarized multiprobe feed radial line slot array, IEEE AP-S (1998), 1184–1187.
10. M. Sierra-Castañer, Contribución a las Técnicas de Diseño y Análisis de Antenas de Ranuras sobre placas paralelas, Doctoral Dissertation, Universidad Politécnica de Madrid, 2000.
11. M. Sierra-Castañer, M. Vera-Isasa, M. Sierra-Pérez, J.A. García, and J.R. Rey, Analysis and design software for radial slot antennas, ANTEM '98, 1998, pp. 337–340.

NUMERICAL ASSESSMENT OF MULTIFREQUENCY MICROWAVE RADIOMETRY FOR SENSING MALIGNANT BREAST CANCER TUMORS

Magda El-Shenawee
Department of Electrical Engineering
University of Arkansas
Fayetteville, AR 72701

Received 30 August 2002

ABSTRACT: *A numerical study of microwave radiometry for malignant breast cancer tumors is presented. The numerical results show that the brightness temperature of malignant tumors exhibits a resonant behavior versus the frequency. The brightness magnitude decreases with the tumor burial depth, however, the resonance frequencies depend only on the tumor's size and material and are independent of the burial depth.* © 2003 Wiley Periodicals, Inc. Microwave Opt Technol Lett 36: 394–398, 2003; Published online in Wiley InterScience (www.interscience.wiley.com). DOI 10.1002/mop.10774

Key words: *radiometry; breast cancer; computational EM; multifrequency; reflectivity*

1. INTRODUCTION

Recently, microwave radiometry has shown potential promise in several subsurface sensing applications [1–3]. Numerous work on using multifrequency microwave radiometry has been published [2, 3, 8]. In the current work, emphasis will be placed on the numerical evaluation of brightness temperature for malignant breast cancer tumors and its behavior as a function of frequency.

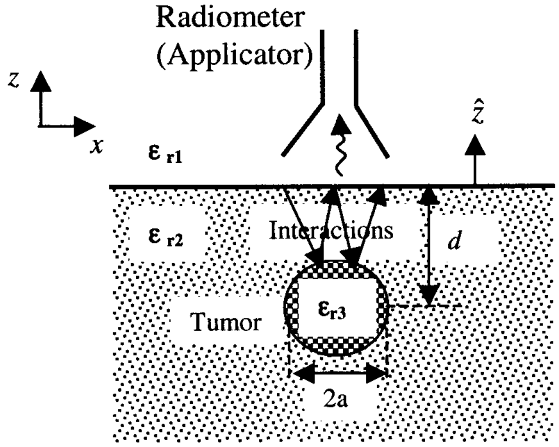

Figure 1 Cross section of a spherical tumor buried beneath a flat air-breast interface showing the multiple interactions mechanism with $n = 2$

The basic idea of using microwave radiometry in breast cancer detection involves measuring the natural electromagnetic radiation or emission from the female breast at microwave frequencies. This electromagnetic radiation changes considerably with the presence of malignant breast cancer tumors [4–8]. In particular, the thermal activity of the female breast is a measure of the tumor growth rate, which can provide information even beyond the physical parameters of the tumor such as its size, material, and location [6]. In [4], the authors presented results based on 618 normal female patients to show the temperature symmetry between the left and right breasts. Therefore, the temperature deviation between the left and right breasts is often used to diagnose the breast cancer in one breast [4–6].

As presented and shown in [4–6], medical microwave radiometry has a number of advantages, such as early diagnosis of the cancer even before the tumor mass contrast is formed, the non-invasiveness of the technique, the absolute harmlessness for patients of all ages, and the range (3–10 cm) of tumor burial depth. However, there are some barriers in this technique: mainly, the required sensitivity of the receiving antenna due to the small number of received thermal signals relative to the surrounding noise signals [4–6].

The objective of this work is to computationally evaluate the brightness temperature as a function of the frequency, tumor size, burial depth, and location. The output of this study can be used to understand the thermal radiation phenomenon, which will aid in designing enhanced radiometers for early detection of breast cancer. The multiple interaction model combined with the fast computational technique, the steepest descent fast multipole method (SDFMM), [9–10] is used here to compute the reflectivity, and hence the brightness temperature, due to the presence of a malignant tumor in the breast.

The geometry of the problem is depicted in Figure 1, where the breast surface is assumed flat and the tumor is modeled as a sphere of radius a and buried at depth d measured from its center. The figure shows the position of the radiometer (applicator) in the near zone to the breast and it shows also the multiple interactions mechanism between the tumor and the breast surface. For simplicity, the thickness of breast skin layer and any interior breast inhomogeneities are not accounted for in this model. Curve-fitted data for electrical properties of the malignant tumor and normal breast tissues are plotted in Figure 2 versus the frequency range

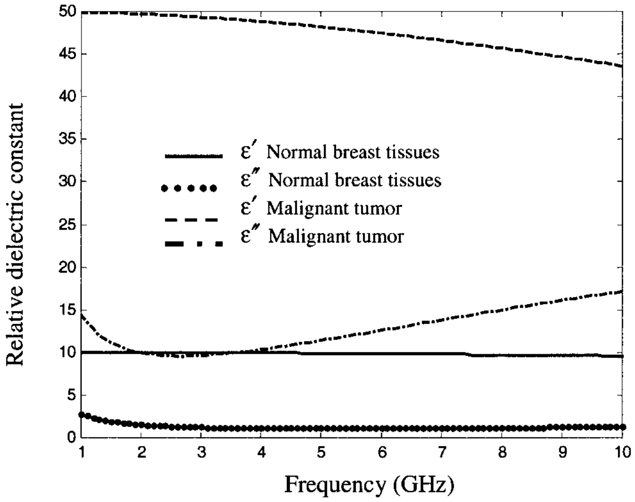

Figure 2 The relative dielectric constant ($\varepsilon_r = \varepsilon' - j\varepsilon''$) vs frequency for the normal and malignant breast tissues obtained using equation 1 in Ref. [20]

1–10 GHz. These results are based on published experimental measurement data [11].

2. FORMULATION

The brightness temperature T_B of an isothermal medium is given by [1, 3]:

$$T_B(\vartheta, \varphi, p, f, \varepsilon_{r2}, \varepsilon_{r3}, g) = T_s(1 - \Gamma), \qquad (1)$$

where the angles ϑ and φ are radiometer observation elevation and azimuth angles, respectively, f is the radiometer observation frequency, p is the polarization of the radiometer (horizontal h or vertical v), ε_{r2} is the dielectric constant of the medium, ε_{r3} is the dielectric constant of the buried object, and g represents the object geometrical dimensions. The total reflectivity of the medium with buried object is represented by Γ, while the physical temperature of the medium and the object is expressed by T_s [2].

The power reflection coefficient or reflectivity Γ and the transmissivity Υ are defined as the normal components of the time-average Poynting's vectors given by [1]:

$$\Gamma = \frac{\hat{z} \cdot \bar{S}_{ar}}{-\hat{z} \cdot \bar{S}_{ai}}, \qquad (2a)$$

$$\Upsilon = \frac{\hat{z} \cdot \bar{S}_{at}}{\hat{z} \cdot \bar{S}_{ai}}, \qquad (2b)$$

where $\bar{S}_a = \mathrm{Re}(\bar{E} \times \bar{H}^*)/2$ is the time-average Poynting vector. The subscripts r, t, and i represent reflected, transmitted, and incident waves, respectively, and $\hat{z}$ is a unit vector normal to the flat interface, as shown in Figure 1. In the case of semi-infinite medium with no buried object, reflectivity and transmissivity can be obtained in closed forms [1]. In this case, they become functions of the reflection and transmission coefficients upon illuminating the semi-infinite flat interface with plane waves [1, 2].

However, the current problem is different due to the presence of a buried object (the tumor) in the flat medium (the breast). The idea here is to computationally evaluate Eqs. (2a) and (2b) to obtain the reflectivity and transmissivity, respectively, of the whole scatterer (the medium with the buried object). In this case, the air-flat interface is modeled with a truncated square surface [9, 10] and, to eliminate the edge excitations, an incident Gaussian beam is employed. The Gaussian beam is basically is a summation of plane waves tapered towards the surface edges [9, 10]. The size of the truncated surface and the incident half-beam width should be much larger than the buried object. The total brightness temperature is reformulated to account for the buried object as follows [2]:

$$T_B(\vartheta, \varphi, p, f, \varepsilon_{r2}, \varepsilon_{r3}, g) = T_s(1 - \Gamma_{surf} - P^r_{obj}/P^i), \qquad (3a)$$

where the subscripts $surf$ and obj indicate the interface surface and the buried object, respectively. The total incident power is given by P^i, the power reflected due to the object only is P^r_{obj}, and Γ_{surf} is the reflectivity of the flat surface with no buried object. The multiple interaction model presented in [10] is used here to compute the equivalent surface currents on the air-medium interface. These currents can be decomposed into two quantities; one is due to the external excitation and the second is due to the multiple interactions with the tumor (see Fig. 1). The deviation in brightness temperature due to the presence of the tumor is expressed as [2]:

$$\Delta T_B(\vartheta, \varphi, p, f, \varepsilon_{r2}, \varepsilon_{r3}, g) = -T_s(P^r_{obj}/P^i). \qquad (3b)$$

The surface currents due to interactions with the tumor are used to compute the reflected power P^r_{obj} and hence to obtain the deviation in brightness temperature [12]. In practice, this deviation represents the differential in temperature between the left and right breasts used to detect the cancer [4–6].

3. NUMERICAL RESULTS

In example 1, the reflectivity Γ and transmissivity Υ of a lossless flat medium with no buried object are computed. The relative dielectric constant is assumed to be $\varepsilon_r = 2.55$ and the truncated surface is assumed to be 240 cm $\times$ 240 cm. The incident and observed waves are assumed to be in normal direction for all cases in this section. The objective of this example is to validate the numerical computations of reflectivity and transmissivity obtained using the SDFMM with those obtained using the closed forms for semi-infinite medium excited with plane waves [1]. The ratios of the time-average power densities in Eqs. (2a) and (2b) are computed using the SDFMM with resolution of 1.2 cm [9, 10, 12]. Briefly, the calculated surface currents on the flat medium are used to radiate electric and magnetic fields at 3 cm above and below the interface. No dependency on this distance is observed in the reflectivity or transmissivity for lossless medium. For lossy medium, the fields are compensated with the attenuation factor. However, smaller distances affected the accuracy of the near-field calculations [12]. The medium reflectivity and transmissivity are plotted in Figure 3 versus the x direction at $y = 120$ cm. Excellent comparison is shown within a square spot of 150 cm $\times$ 150 cm centered at $x = 120$ cm, $y = 120$ cm, which is the center of the Gaussian beam footprint. As shown in Figure 3, the beam width is $2W = 96$ cm, which implies, as expected, that plane waves can be assumed within the spot area of $2W \times 2W$. The reflectivity and transmissivity are added up to unity, as shown in Figure 3. Moreover, at normal incidence, the results for the vertical or horizontal polarizations are similar.

In Figure 4, the same data of the previous example is used and a comparison is shown for reflectivity and transmissivity, but in this case for a slightly lossy medium. The relative dielectric constant here is $\varepsilon_r = 3.55 - j0.4$ (loamy soil with 5% moisture

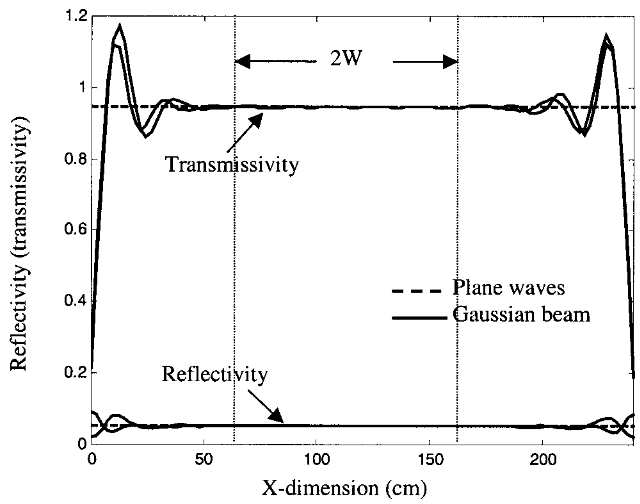

Figure 3 Reflectivity and transmissivity of a lossless flat medium with relative dielectric constant $\varepsilon_r = 2.55$. The solid curves represent the SDFMM results for both the vertical and horizontal polarizations and the dotted curves represent the closed forms of the semiinfinite medium

[1]). Because the computed time-average power densities are obtained at 3 cm below the interface (as previously explained), the field values in this case are multiplied by $\exp(2\alpha l)$, where α is the medium attenuation constant and $l = 3$ cm. The computed results show excellent agreement with the closed forms in [1] and also within the same spot area $2W \times 2W$, similar to the previous lossless case.

In Figure 5, the reflectivity and transmissivity of normal breast tissues with relative dielectric constant $\varepsilon_r = 10 - j1.2$ are computed (see Fig. 2 and [11]). Notice that the normal breast tissues have almost the same dielectric constant in the microwave frequency range 1–10 GHz. The results are plotted versus the x direction per wavelength and at $y = 4\ \lambda_0$. The modeled surface dimensions are $8\ \lambda_0 \times 8\ \lambda_0$, where λ_0 is the free space wavelength. Also in this example, the computed values of the transmitted fields are multiplied by $\exp(2\alpha l)$, with $l = 0.1\ \lambda_0$, the near field resolution is $0.04\ \lambda_0$, and the half-beam width is $W = 1.6\ \lambda_0$. The reflectivity and transmissivity, upon compensation with the attenuation factor, are added up to unity as shown in Figures 4 and 5. The reflectivity in Figure 5 is larger than that in Figures 3 or 4, which is due to the larger dielectric constant of the medium, in this case $10 - j1.2$, as shown in Figure 2. As expected, the transmissivity in Figure 5 is smaller than that in Figures 3 or 4, due to the larger conductivity of the medium in this case. Notice the slight oscillations in the transmissivity and reflectivity in Figure 5, which are due to the increase of edge reflections in this case. This could be decreased by increasing the Gaussian beam tapering, that is, decreasing W [9, 10].

In Figures 3–5, a validation is demonstrated by computing the reflectivity and transmissivity using the SDFMM. In Figure 6, the time-average reflected power density $\bar{S}_{ar}$ due to only the malignant tumor is plotted versus the x direction at $y = 4\ \lambda_0$. The malignant tumor is modeled by a sphere of radius $a = 5$ mm and is buried at depth of $d = 2$ cm, measured from its center as depicted in Figure 1. The dielectric constant of the malignant tumor varies with frequency as shown in Figure 2, while the dielectric constant of the normal breast tissues is assumed constant as $\varepsilon_r = 10 -$

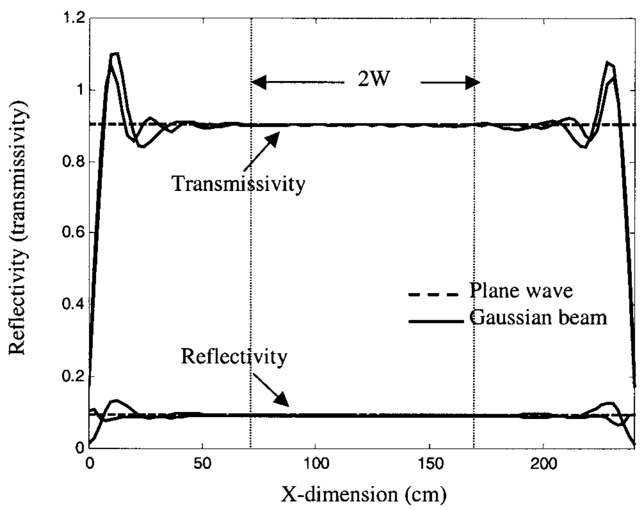

Figure 4 The reflectivity and transmissivity of a slightly lossy flat medium with no buried object and relative dielectric constant $\varepsilon_r = 3.55 - j0.4$ (Loamy soil with 5% moisture [1])

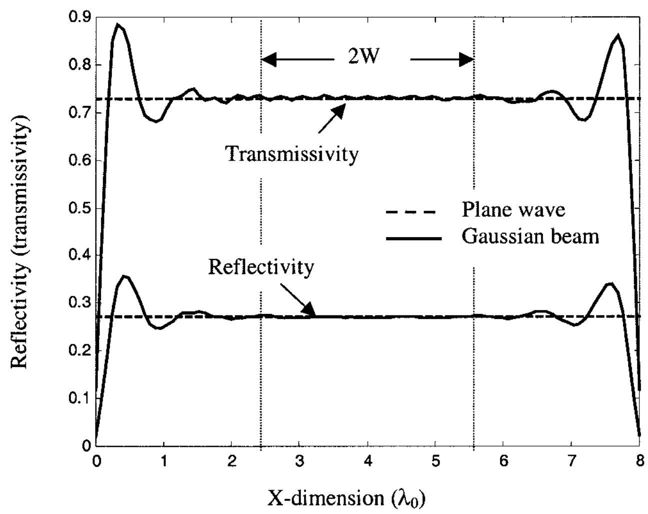

Figure 5 The reflectivity and transmissivity of normal breast tissues with relative dielectric constant of $\varepsilon_r = 10 - j1.2$ (see Fig. 2 and [20])

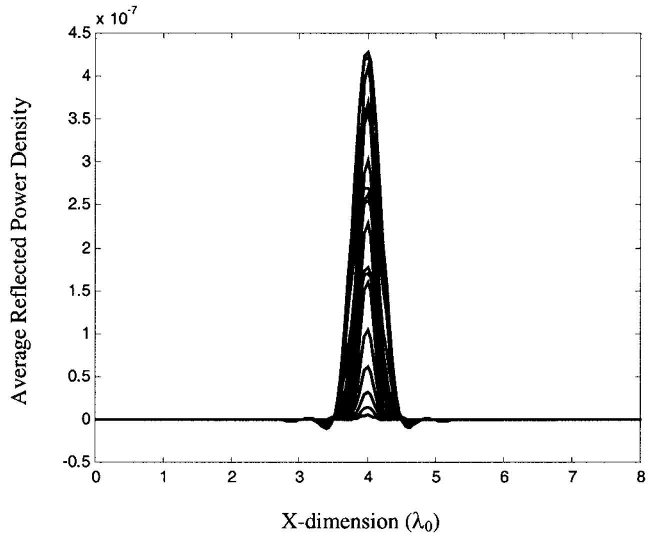

Figure 6 The time-average reflected power density of the malignant tumor only versus the x-direction

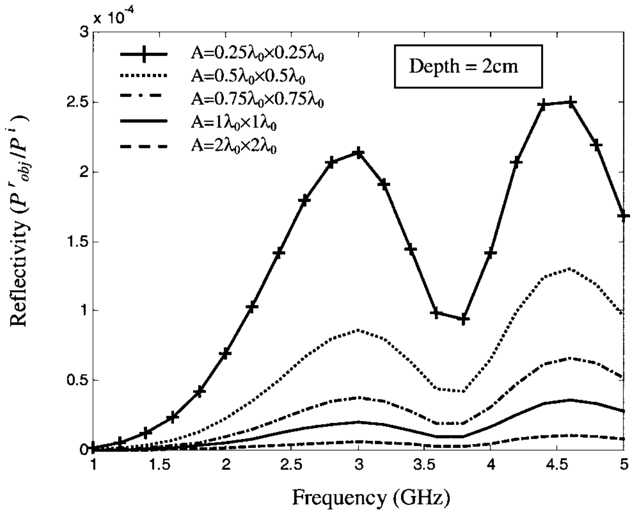

(a)

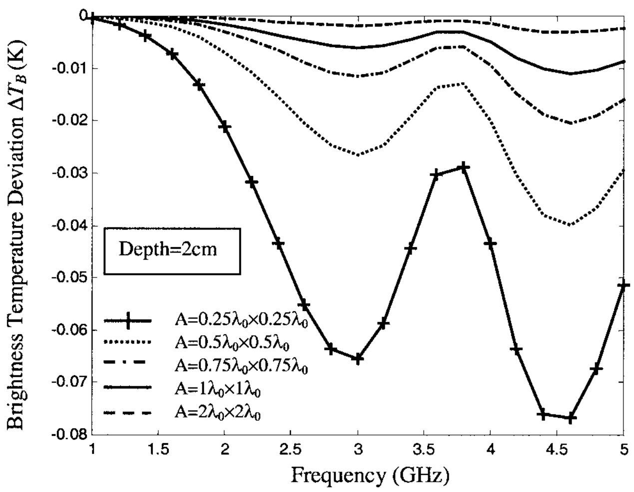

(b)

Figure 7 (a) The reflectivity of malignant tumor versus frequency. The tumor radius is $a = 5$ mm and it is buried at depth of 2 cm measured from its center (see Fig. 1); (b) Brightness temperature deviation ΔT_B due to the presence of malignant tumor of radius $a = 5$ mm buried in normal breast tissues for same data of Fig. 7a

$j1.2$. The frequency ranges from 1–5 GHz in steps of 200 MHz, which implies that there are 21 curves plotted in Figure 6. Notice that the dimension of the plane-wave square-spot area, as shown in Figures 3–5, ranges from 96 cm to 19.2 cm. This area is considered much larger than the diameter of the tumor, which is 1 cm in this case. The purpose of Figure 6 is to show that the waves reflected due to the tumor are sensed within the spot area of $2W \times 2W$ for all considered frequencies. The tumor reflected waves are spherical waves as discussed in [2].

The emphasis of the following examples is to demonstrate the behavior of thermal emissivity or tumor brightness temperature versus frequency. Therefore, in Figure 7, the reflectivity due to the tumor is plotted versus the frequency from 1–5 GHz in steps of 200 MHz. The tumor radius and burial depth are 5 mm and 2 cm, respectively. The tumor reflectivity is obtained by computing the term (P^r_{obj}/P^i) in Eq. (3b), which is obtained by integrating the time-average reflected power density $\bar{S}_{ar}$ due to the tumor and the time-average incident power density $\bar{S}_{ai}$ of the Gaussian beam over the radiometer cross section area A, where $A \leq 2W \times 2W$, as explained in Figures 3–5. As an example, the radiometer cross section was 1 cm × 2.3 cm at 3.3 GHz in [4]. As expected, the total reflected power P^r_{obj} depends on the cross section area A of the receiving antenna (the radiometer or applicator) as shown in Figure 7(a). For simplicity, the radiometer cross section is assumed to be a square with dimension ranging from 0.25 λ_0 to 2 λ_0. The results clearly show the oscillatory behavior of tumor reflectivity versus frequency, with peaks occurring at 3 GHz and 4.5 GHz. Also, the results show that the smaller the observing area A, the larger the magnitude of the sensed tumor reflectivity. Upon multiplying the reflectivity of Figure 7(a) with the physical temperature T_s, the deviation in brightness temperature due to the presence of the tumor is shown in Figure 7(b). The physical temperature of breast tissues vary with a woman's age, for example, at 50 years of age, the average temperature of the breast is assumed to be 33.7°C (or 306.85 K), as reported in [5]. Naturally, the tumor's physical temperature is different form the surrounding normal breast tissues because they vary in material, as shown in Figure 2. However, in this work it is assumed that the physical temperature T_s in Eqs.

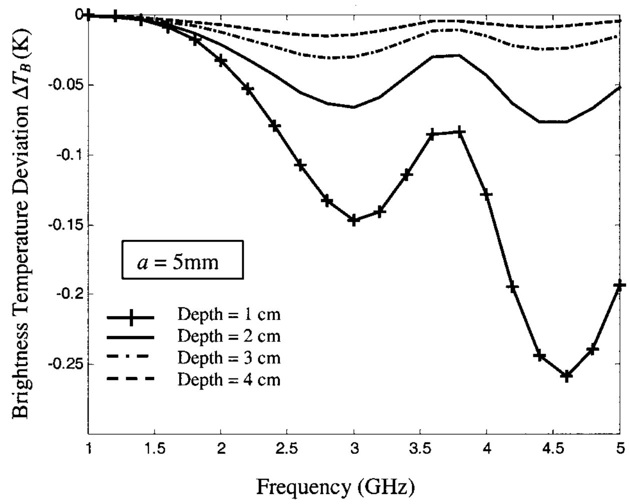

(a)

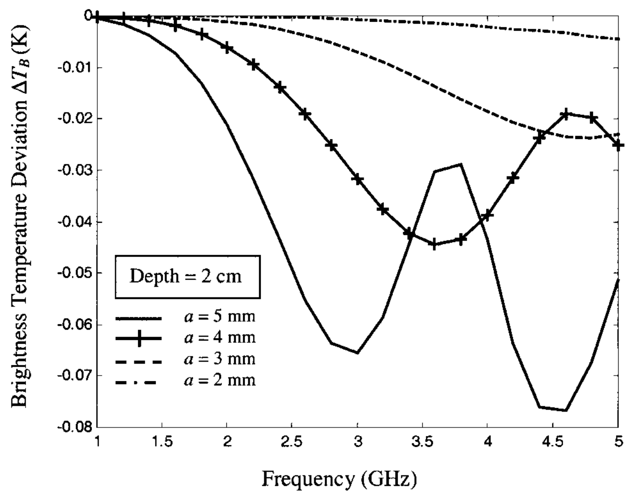

(b)

Figure 8 (a) Brightness temperature deviation ΔT_B due to the presence of malignant tumor in normal breast tissues. The radiometer cross section is assumed as $A = 0.25\ \lambda_0 \times 0.25\ \lambda_0$; (b) Deviation in brightness temperature ΔT_B due to the presence of malignant tumor in normal breast tissues. The radiometer cross section area is $A = 0.25\ \lambda_0 \times 0.25\ \lambda_0$

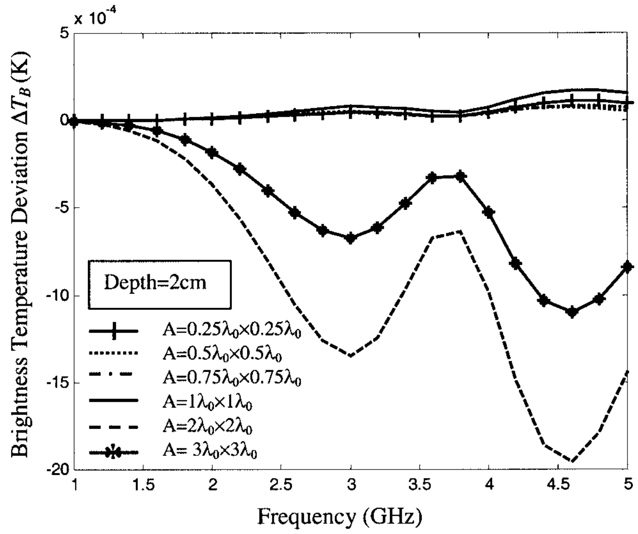

Figure 9 Deviation in brightness temperature ΔT_B due to the presence of malignant tumor in normal breast tissues. The tumor radius is $a = 5$ mm and is located at (3.2 λ_0, 4.8 λ_0). The radiometer cross section area A is centered as (4 λ_0, 4 λ_0)

(3a) and (3b) is the average temperature for the breast, which is reported for a variety of ages in [5].

In Figure 8(a) and (b), a parametric study for the brightness temperature deviation ΔT_B is investigated versus the frequency with the radiometer cross section area $A = 0.25\ \lambda_0 \times 0.25\ \lambda_0$. In Figure 8(a) ΔT_B is plotted for several burial depths of 1–4 cm, where the tumor radius a is assumed to be 5 mm. The results show that the brightness temperature oscillates at the same frequencies regardless of the burial depth. However, the brightness magnitude decreases with the burial depth increase, due to the large attenuation in normal breast tissues at microwave frequencies. In Figure 8(b), ΔT_B is plotted for several tumor radii of 2–5 mm, buried at the same burial depth of 2 cm. The results clearly show the brightness oscillating behavior for all sizes, however, for larger tumor radius the temperature peaks at lower frequencies and vice versa.

In all examples above, the tumor was buried in the center of the modeled breast at 4 λ_0, 4 λ_0. In this example, the tumor is buried off center at 3.2 λ_0, 4.8 λ_0, in the upper left quadrant of the breast. The tumor radius is $a = 5$ mm and is buried at 2 cm. The deviation in brightness temperature ΔT_B is plotted in Figure 9 for several radiometer square cross section areas with dimensions ranging from 0.25 λ_0 to 3 λ_0. The results show that the brightness temperature increases with the increase of the cross section area up to $A = 2\ \lambda_0 \times 2\ \lambda_0$ and after that it starts to decrease. This observation contradicts the results of Figure 7(b), where the brightness temperature increases with the decrease of A. The reason of this contradiction is that in Figure 7(b) both the tumor and radiometer cross section are located at the center of the modeled breast. However, in Figure 9, the radiometer location is kept in the breast cancer, while the tumor is moved to the breast upper left quadrant at 3.2 λ_0, 4.8 λ_0. This implies that for values of A smaller than 1.6 $\lambda_0 \times$ 1.6 λ_0, the radiometer does not sense the tumor because it is located outside this area. After experimentation with the radiometer location, the results show that when it is re-located and centered exactly above the tumor, a greatly enhanced brightness temperature is received. For a cross-section area equal to 2 $\lambda_0 \times$ 2 λ_0, the exact results of Figure 7(b) are obtained. This suggests that scanning the breast surface with a localized radiometer cross section is better than observing the brightness temperature from the whole breast.

4. CONCLUSION

The conducted numerical evaluation for a breast cancer tumor's brightness temperature shows clear oscillatory behavior versus the frequency. The results show that the peaks of brightness temperature occur at the same frequencies regardless of the tumor's burial depth, however, the oscillating frequencies depend on the tumor's size and material. These observations can be used to enhance the radiometer design parameters such as the operating frequency or multiple frequencies, the bandwidth, and the radiometer-receiving cross-section area. This statement is considered a future work in collaboration with the NASA Langley Research Center.

ACKNOWLEDGMENTS

This research was sponsored by the NASA Langley Research Center, grant no. US/NASA/NAG-1-020. The author would like to thank Drs W. Lawrence, J. Johnson, M. Deshpande, and W. Munden at NASA Langley for their valuable discussions. This work is supported in part by NSF-ERC Northeastern University, award number EEC-9986821.

REFERENCES

1. F.T. Ulaby, R.K. Moore, an A.K. Fung, Microwave remote sensing active and passive, volume 1: Microwave remote sensing fundamentals and radiometry, Addison-Wesley, 1981.
2. B. Unga and J.T. Johnson, A study of microwave thermal emission from a sub-surface object, Microwave Opt Technol Lett 36 (2000), 9–12.
3. J.T. Johnson, H. Ki, D. Wiggins, and Y. Cheon, Sub-surface object sensing with a multi-frequency microwave radiometer, IEEE Trans Geosci Rem Sensing, to appear.
4. A.H. Barrett, P.C. Myers, and N.L. Sadowsky, Detection of breast cancer by microwave radiometry, Radio Sci 12 (1977), 167–171.
5. A.V. Vaisblat, S.G. Vesnin, M.A. Konkin, A.V. Lashchenkov, and N.N. Tihomirova, Using microwave radiometry for detection of breast cancer, RES Ltd Radiometry Company Literature Publisher, http://www.resltd.ru/eng/literature/cancer_eng.htm, 2000.
6. K.L. Carr, Microwave radiometry: Its importance to the detection of cancer, IEEE Trans Microwave Theory Techniques 37 (1989), 1862–1868.
7. J. Lee, K. Kim, S. Lee, S. Eom, and R.V. Troitsky, A novel design of thermal anomaly for mammary gland tumor phantom for microwave radiometer, IEEE Trans Biomedical Engineering 49 (2002), 694–699.
8. S. Jacobson and P.R. Stauffer, Multifrequency radiometric determination of temperature profiles in a lossy homogeneous phantom using a dual-mode antenna with integral water bolus, IEEE Trans Microwave Theory and Techniques 50 (2002), 1737–1746.
9. M. El-Shenawee, C. Rappaport, E. Miller, and M. Silevitch, Three-dimensional subsurface analysis of electromagnetic scattering from penetrable/PEC objects buried under rough surfaces: use of the steepest descent fast multipole method (SDFMM), IEEE Trans Geosci & Rem Sensing 39 (2001), 1174–1182.
10. M. El-Shenawee, The multiple interaction model for non-shallow scatterers buried beneath two-dimensional random rough surfaces, IEEE Trans on Geosci & Remote Sensing 40 (2002), 982–987.
11. X. Li and S.C. Hagness, A confocal microwave imaging algorithm for breast cancer detection, IEEE Microwave and Wireless Components Letters 11 (2001), 130–132.
12. C.A. Balanis, Advanced Engineering Electromagnetics, John Wiley & Sons Inc, Ch. 6, pp. 254–309, 1989.